Applied Physics Letters

RESEARCH ARTICLE | OCTOBER 27 2025

Observation of acoustic spin skyrmion in confined sound field with orbital angular momentum

Jia-Yu Zheng ; Wan-Na Chen ; Jing-Yi Lv; Lei Wang; Hua-Feng Xu; Hong-Wei Wu

Appl. Phys. Lett. 127, 172201 (2025)
https://doi.org/10.1063/5.0300884

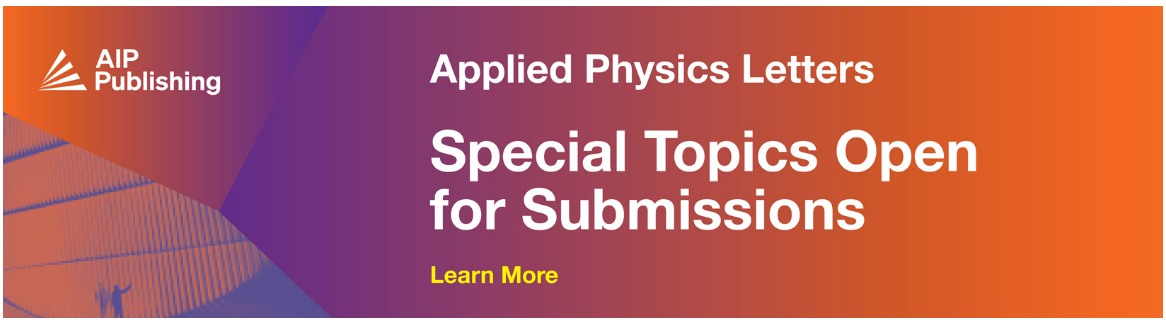

Applied Physics Letters ARTICLE pubs.aip.org/aip/apl

Observation of acoustic spin skyrmion in confined sound field with orbital angular momentum

Cite as: Appl. Phys. Lett. **127**, 172201 (2025); doi: 10.1063/5.0300884
Submitted: 4 September 2025 · Accepted: 6 October 2025 ·
Published Online: 27 October 2025

Jia-Yu Zheng,[1] Wan-Na Chen,[1] Jing-Yi Lv,[1] Lei Wang,[1] Hua-Feng Xu,[1,2] and Hong-Wei Wu[1,2,3,a)]

AFFILIATIONS

[1]School of Mechanics and Photoelectric Physics, Anhui University of Science and Technology, Huainan 232001, China
[2]Center for Fundamental Physics, Anhui University of Science and Technology, Huainan 232001, China
[3]National Laboratory of Solid State Microstructures, Nanjing University, Nanjing 210093, China

[a)]Author to whom correspondence should be addressed: hwwu@aust.edu.cn

ABSTRACT

Topological textures of spin vectors are fundamentally interesting and possess generic features for various vector waves. However, experimental realizations of spin skyrmions are mostly restricted to magnetic materials and optical waves, which remains a significant challenge for airborne sound waves with intrinsic curl-free features. In this work, we propose a concentric cylindrical metastructure to construct spin skyrmion textures with subwavelength scale excited by an acoustic spin source. By acoustic spin-orbital coupling, we achieve multi-order confined Bessel spoof acoustic surface waves with orbital angular momentum on the metastructure surface, experimentally observe the acoustic spin skyrmion configurations with subwavelength scale, and verify the topologically protection for introducing the defects. The achievement of acoustic spin skyrmions not only expands the family of topological textures in sound but also provides an avenue to manipulating small particles by controlling structural acoustic fields.

Skyrmions, as a physical model describing baryons in nuclear physics, were first proposed by Tony Skyrme.[1] Nevertheless, they are flourishing in condensed matter physics and form a topological quasi-particle family, including Néel-type skyrmion,[2] Bloch-type skyrmion,[3] anti-type skyrmion,[4] meron,[5–7] bimeron,[8,9] hopfion,[10,11] and so on. The intrinsic stability and controllability of these topological textures of spin vector fields hold promise for next-generation technologies related to high density information storage and processing. Light, as an important information carrier, naturally attracts great attention for constructing optical skyrmions. The first pioneered optical skyrmion lattice for electric field vectors is experimentally observed in a metal surface,[12] and the confined electromagnetic fields with orbital angular momentum also configure the spin vectorial skyrmion.[13] Since then, the investigation of interesting topological textures has sprung up in optical systems, and multi-physical vector fields (including electric/magnetic fields,[12] spin fields,[14,15] Stokes vectors,[16,17] and energy flow vectors[18]) are constructed to form various topological quasiparticles. In addition, the optical skyrmions also expanded from the classical regime to the quantum realm for generating single-photon skyrmions[19] and non-local skyrmions.[20]

Luxuriant magnetic and optical topological textures not only provide an avenue for advanced information processing but also arouse interesting investigations of skyrmions in other classical waves, such as acoustic waves,[21,22] elastic waves,[23] and water waves.[24,25] In terms of airborne acoustics, the skyrmion textures are configured with the velocity vector fields by designing the metasurfaces. For example, recent experiments have also demonstrated that the acoustic skyrmion and meron lattices can be realized in hexagonal and tetragonal metastructures.[21,26] Comparing with the skyrmion lattices, which require stringent excitation conditions, we further propose acoustic localized skyrmions in a deep-subwavelength metastructure without any restrictions in our previous works.[27–30] Compared with the transverse waves, which hold spin angular momentum naturally, configuring and manipulating spin vector fields for the curl-free sound remain a significant challenge. To explore the polarization and spin in acoustic waves, various sound near fields have recently been theoretically investigated in inhomogeneous acoustic beams and spoof acoustic surface waves (SASWs).[22,31,32] Instinctively, acoustic spin skyrmionic texture may further enrich the vector properties of sound waves and expand the family of acoustic skyrmions.

In this work, we generate multi-order Bessel spoof acoustic surface waves on a concentric cylinder excited by an acoustic spin source. We theoretically analyze the formation mechanism of spin skyrmions, where the energy flux $\mathcal{J}$ of the Bessel spoof acoustic surface wave along the azimuthal direction is accompanied by the reactive power, $\mathcal{R}$, at radial and axial directions to configure the Néel-type spin skyrmion configuration with subwavelength scale. We also perform experiment measurements for the first order spin skyrmionic mode and verify the topological protection for introducing defects. Furthermore, to improve the quality of the spin skyrmionic mode, we also propose a scheme that lifts the hard boundary at the structure edge to modify the quality factor of the Bessel SASW and find that the hard boundary can effectively enhance the quality of the lower-order spin skyrmion. Our results not only expand the family of acoustic skyrmions but also hold great promise for manipulating small particles with subwavelength structural acoustic fields.

At first, we implement the skyrmion mode of the acoustic spin field by designing a three-dimensional (3D) concentric cylinder. As shown in Fig. 1(a), the structure is composed of twelve layers of concentric rings nested with a height of $H = 5$ cm, and the outer radius and inner radius are $r_1 = 5$ cm and $r_2 = 1.6$ cm, respectively. The thickness of each layer of the ring is 0.1 cm, the groove width is $a = 0.2$ cm, and the period is $b = 0.3$ cm, as shown in the inset of Fig. 1(a). Four point sources are set up at the center of the structure, and by adjusting their phases ($\varphi_1 = 0$, $\varphi_2 = \pi/2$, $\varphi_3 = \pi$, and $\varphi_4 = 3\pi/2$) to form a counterclockwise spin source, which excites an acoustic vortex to couple the metastructure surface for forming the Bessel SASWs based on spin-orbital coupling, its pressure field can be expressed as[33]

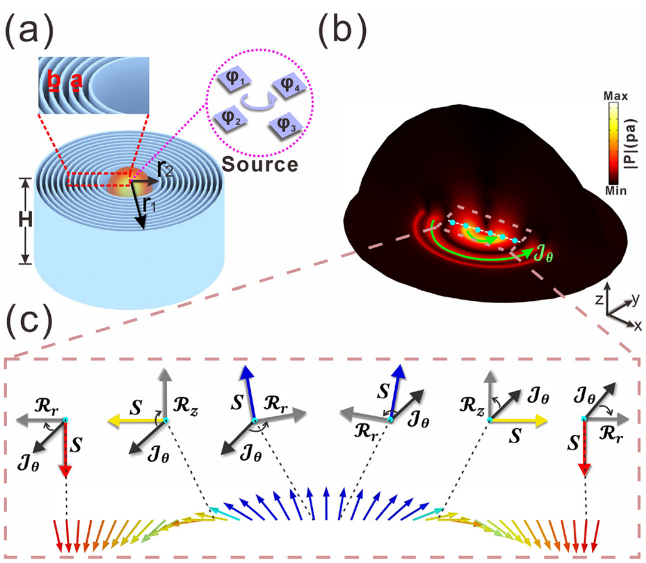

FIG. 1. A schematic diagram of the structure and local vector orientation for forming the Néel-type spin skyrmion. (a) Three-dimensional structure diagram, where H represents the structural height, r_1 and r_2 denote the inner and outer radii, respectively. The illustration shows the wall spacing a and the channel period b. The four point sources set in the center of the structure are shown in the dashed circle. (b) The distribution of the sound pressure field in the $x-z$ and $x-y$ planes. Along the azimuthal direction, the green arrows are a series of donut-shaped energy fluxes. (c) The variation of the local spin field vectors along the radial direction corresponds to the area within the dashed box in (b). The black arrows represent the direction of energy flux, the gray arrows show the reactive power vectors, and the arrows that gradually change from red to blue are the spin vectors.

$$p = p_0 J_l(kr) e^{il\theta} e^{-k_z z} e^{-i\omega t}, \tag{1}$$

where p_0 is the amplified of acoustic pressure field, $J_l(\cdot)$ corresponds to the l-order the first kind of Bessel function, and $l = 1$ refers to topological charge corresponding to the counterclockwise spin source. $\omega = c k_0$ is angular frequency, $c = 343$ m/s for air sound speed. $k_z = \sqrt{k^2 - k_0^2}$, and k and k_z are wave numbers corresponding to in-plane and out-of-plane directions in cylindrical coordinates (r, θ, z). In the metastructure, a periodic groove structure along the radial direction will induce the dispersive relationship as $k = k_0\sqrt{1 + \left[\frac{a}{b}/\tan\left(\frac{k_0 H + \pi}{2}\right)\right]^2}$.[34] Based on Eq. (1) and $\boldsymbol{v} = \frac{1}{i\omega\rho}\nabla p$ (ρ is the air mass density), we can produce the time-averaged energy flux $\mathcal{J} = \frac{1}{2}\mathrm{Re}[p^* \boldsymbol{v}]$ in the azimuthal direction as a series of donut-shaped distributions shown by the green arrows in Fig. 1(b), $\mathrm{Re}[\cdot]$ is the real part, and $\boldsymbol{v}$ is the acoustic velocity vector field on the structure's surface. Similarly, the reactive power vector can be expressed as $\mathcal{R} = \frac{1}{2}\mathrm{Im}[p^* \boldsymbol{v}]$ along the radial and z directions, where $\mathrm{Im}[\cdot]$ is the imaginary part. Consequently, a general geometrical relation for the acoustic spin density formed on the surface of the structure can be expressed as[33]

$$\boldsymbol{s} = \frac{4\rho}{\omega|p|^2}\mathcal{J} \times \mathcal{R}. \tag{2}$$

The energy flux plays an important role in the acoustic spin skyrmion formation. For confined Bessel SASW, the surface Poynting vector has only azimuthal direction $\mathcal{J}_\theta$ as shown as the green arrows related to a series of donut-shaped energy flux in Fig. 1(b). However, the reactive power vector corresponding to the variation of the energy flux density has two components ($\mathcal{R}_r$ and $\mathcal{R}_z$), the z-direction component $\mathcal{R}_z$ induces a spin density component s_r, while the radial direction component $\mathcal{R}_r$ will induce a spin density component s_z. To illustrate the relationship, we also pick the three vectors along the diameter of the structure covering the first donut as a dashed box in Fig. 1(c) by numerical calculation. We find that the right-handedness is satisfied among the spin vectors $\boldsymbol{s}$, the energy flux $\mathcal{J}$, and the reactive power vector $\mathcal{R}$ corresponding to these positions, as shown in the upper part of Fig. 1(c), the spin vectors clearly showcase a Néel-type skyrmionic distribution.

Based on the above-mentioned analysis, we perform numerical calculations to verify the generation of spin skyrmion by using the commercial software COMSOL Multiphysics in a pressure acoustic module of frequency domain. We observe the vector distribution of the first-order and second-order spin skyrmions at 3270 and 3400 Hz, respectively, as illustrated in Figs. 2(a) and 2(d); the higher order skyrmionic modes are presented in the supplementary material. Here, we define the nth-order skyrmionic mode as including n intact donuts in the structure's surface. The top and bottom surfaces exhibit dispersed and converged configurations accordingly, due to the opposite reactive power directions. The topological property of a skyrmion can be characterized by the skyrmion number N_{sk}, which can be defined as

$$N_{sk} = \frac{1}{4\pi}\iint \hat{\boldsymbol{s}} \cdot \left(\frac{\partial \hat{\boldsymbol{s}}}{\partial x} \times \frac{\partial \hat{\boldsymbol{s}}}{\partial y}\right) dx\, dy, \tag{3}$$

where $\hat{\boldsymbol{s}} = \frac{\boldsymbol{s}}{|\boldsymbol{s}|}$. The N_{sk} of the first-order and second-order spin skyrmionic modes are $N_{sk1} = 0.8625$ and $N_{sk2} = 0.9373$ by numerical

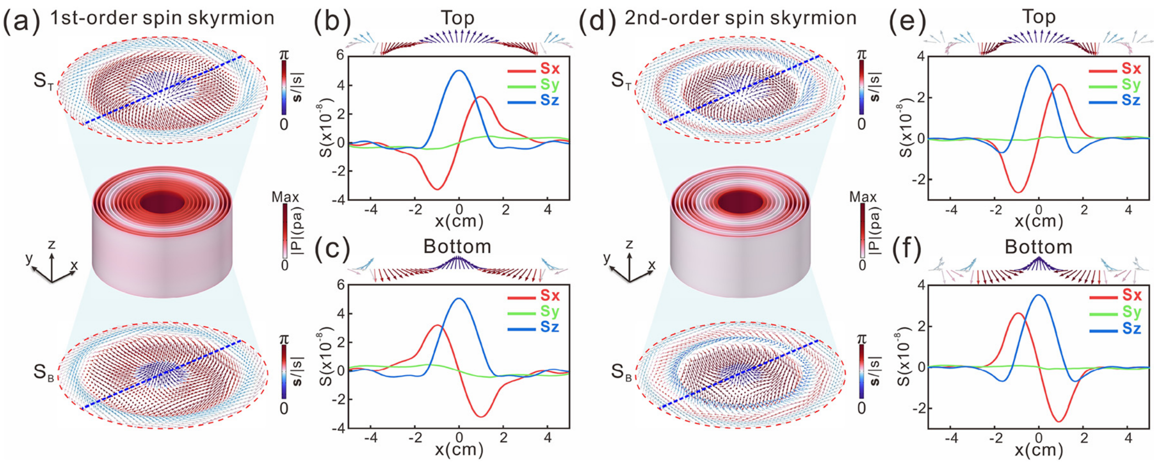

FIG. 2. The simulation results of first-order and second-order Néel-type skyrmion modes formed by the acoustic spin field. (a) and (d) Schematic of the simulation results for the absolute value of the sound pressure and the vector distribution of the spin field for the first-order and second-order spin skyrmion modes, respectively. The direction of the spin field vector is indicated by arrows. (b) and (c) The distribution of first-order spin vector arrows along the blue dashed lines on the top (S_T) and bottom (S_B) surfaces and corresponding spin components. (e) and (f) The distribution of second-order spin vector arrows on the top and bottom surfaces of the structure and corresponding spin components.

simulation, respectively. The results indicate that the skyrmion number of the first-order spin skyrmion is slightly different from the theoretical value of 1, but the second-order skyrmion number is close to the theoretical value. This phenomenon can be attributed to the distribution of the first-order mode with a larger mode volume and lower Q factor. The formation of the first-order spin skyrmion mode will be further improved and analyzed in a later section. Figures 2(b) and 2(c) show the spin field distribution of the first-order skyrmion and spin components (s_x, s_y, s_z) on the top and bottom surfaces, respectively, which correspond to the blue dashed line in Fig. 2(a). We find that the direction of the spin field vector is vertically upward at the center of the structure when the longitudinal component (s_z) is the largest. During the expansion from the center of the structure to the edge, the s_z gradually decreases to a minimum, at which point the transverse component (s_x) will reach a maximum, where the spin vector arrow flips to the horizontal direction. Subsequently, the longitudinal component increases slowly while the transverse component decreases, and this process is not obvious in the graphs because of the large longitudinal component at the center. Similarly, Figs. 2(e) and 2(f) show the second-order spin vector field distribution and individual components of the spin field vector on a line radially along the top and bottom surfaces of the structure, respectively.

Above, we have theoretically analyzed and numerically calculated the realization of the skyrmion mode in the acoustic spin field. Next, we will experimentally observe the distribution of the first-order spin skyrmion mode supported on the top surface of the structure. A photograph of a concentric cylindrical sample with resin material made by 3D printing is shown in Fig. 3(a), in which four speakers are inserted from the perimeter of the sample to the center of the structure. The speakers are used to excite by means of a connection to a syringe and needle, thereby directing sound waves to the center of the structure. The phases of the four speakers are numbered as φ_n $(n = 1, 2, 3, 4)$. When the phases of the four speakers are set to $\varphi_1 = 0$, $\varphi_2 = \pi/2$, $\varphi_3 = \pi$, and $\varphi_4 = 3\pi/2$, respectively, according to Fig. 1(a), a

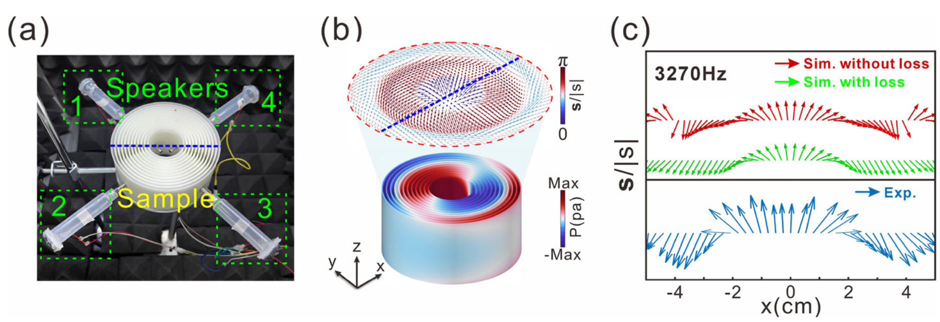

FIG. 3. Acoustic skyrmion simulation and experimental measurement of spin field distribution. (a) Schematic diagram of the experimental setup. The numbers 1–4 represent the serial numbers of the four speakers, corresponding to phase settings as φ_n $(n = 1, 2, 3, 4)$. (b) Simulation diagrams of the structural sound pressure field distribution and the skyrmion mode formed by the spin field. The direction of the spin field is indicated by arrows. (c) Simulation without loss (red arrows) and with loss (green arrows), the experimental (blue arrows) spin field skyrmion modes are indicated by arrows along the blue dashed line in (b). The operating frequencies of both the simulation and the experiment are 3270 Hz.

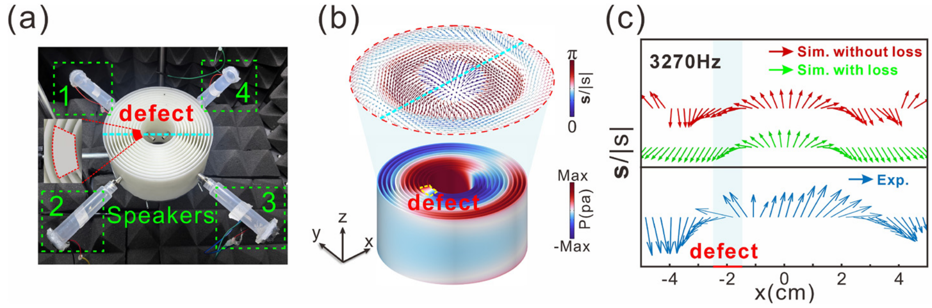

FIG. 4. Robustness experiment of the acoustic spin skyrmion. (a) Schematic diagram of the robustness experimental setup. The numbers 1–4 represent the serial numbers of the four speakers, corresponding to phase settings as φ_n ($n = 1, 2, 3, 4$). The inset is an enlarged view of the defect region. (b) Simulation diagram of the skyrmion mode formed by the acoustic spin field. The yellow areas show the positions of the defect in the sound pressure field and the spin field, respectively. (c) Simulation without loss (red arrows) and with loss (green arrows), the experimental (blue arrows) results of the spin field distribution with the defect, along the blue dotted line in (b). The operating frequencies for both simulation and experiment are 3270 Hz.

counterclockwise spin source can be realized. Figure 3(b) shows the simulation results of the acoustic pressure field distribution and the spin field vector distribution on its top surface without loss. Since the resin material is slightly shaken during the experiment, the presence of losses will change the phase of the reflection at the edges of the structure, affecting the texture distribution near the edges. In order to match the loss due to the experimental environment, we also calculated the results with losses, as shown by the green arrow distribution in Fig. 3(c).

During the experiment, the sine wave signal is generated by the signal generator (AFG1022, Tektronix), amplified in the power amplifier (CPA2400, SinoCinetech), and passed through a splitter box (FM02-12D, Tatsukawa) to drive the speaker. We use a WL-AVS-3D vector microphone[21] to measure the acoustic pressure and velocity (v_x, v_y, and v_z) distribution above the surface of the sample along the blue dashed line in Fig. 3(a). The magnitude and direction of the corresponding acoustic spin field that can be obtained from experimental measurements are given according to Eq. (2).[33] The results of numerical simulations and experimental measurements of the spin field distribution along the diameter on the sample surface are shown in Fig. 3(c). The red and green arrows at the top show the simulation results without and with losses, respectively, and the blue arrow at the bottom shows the results of the experiment. It can be seen that the direction of the spin field is continuously flipped from 0 to π along the longitudinal direction, which is consistent with the simulated results and proves the first-order spin skyrmion mode.

It is well known that topological textures are protected against structural defects and disorder in real space. To observe the robustness of the spin skyrmion mode, we intentionally introduce the defect in the symmetric structure to block the channel by inserting pieces of stiff paper into the locations where defects needed to be created. Additionally, white adhesive tape was applied to the surface of the structure to seal the grooves, as shown in the red region in Fig. 4(a). We simulate the sound pressure field and spin field distributions of the skyrmion mode, as shown in Fig. 4(b). The results indicate that even though the surface acoustic pressure field changes somewhat, the introduction of the defect has little effect on the spin field distribution, which changes only slightly in the vicinity of the defect. The measured experimental results in Fig. 4(c) agree with the simulated results and confirm the robustness of the skyrmion configuration.

As mentioned in Fig. 2, the first-order spin skyrmion mode with the low Q factor is imperfect due to the evanescent field at the

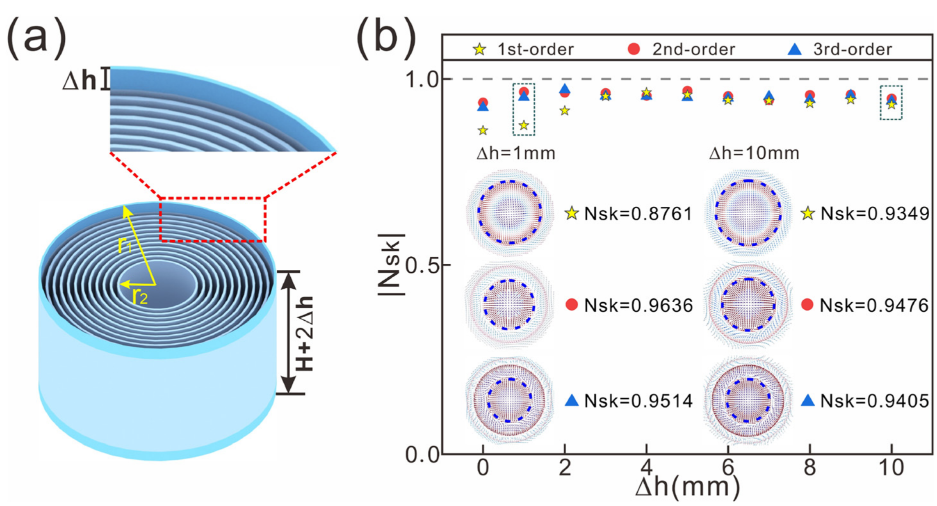

FIG. 5. The effect of hard boundary beyond the surface of the structure on the first-order spin skyrmion. (a) Schematic diagram of the structure with the outermost ring added to the hard boundary. (b) Impact of hard boundary height to the skyrmion number on the top surface of the structure. The insets show the spin field vector distribution for hard boundaries of 1 and 10 mm, respectively. The blue dashed circle denotes the integration region of the skyrmion number.

structure boundary. Therefore, we propose a scheme to lift the hard boundary of the outermost ring beyond the surface of the structure to change the reflection phase at the edge for increasing the Q factor of the first-order skyrmion mode, as shown in Fig. 5(a), Δh is the height beyond the structure surface. To analyze the influence of the hard boundary on the skyrmion modes, we calculate the skyrmion numbers, as shown in Fig. 5(b). The pentagrams, circles, and triangles in the diagram represent the first-order, second-order, and third-order skyrmion modes, respectively. By increasing the height of the hard boundary, we can observe a significant increase for the skyrmion number of the first-order mode from $N_{sk} = 0.8761$ to $N_{sk} = 0.9349$ when Δh increases from 1 to 10 mm. While the second- and third-order skyrmionic modes with high Q factors are insensitive to the boundary condition. In fact, when the height of the hard boundary increases to 3 mm, the stable mode with a high Q factor (which is discussed in Fig. S4 in the supplementary material) has been formed for the first-order spin skyrmion, which holds $N_{sk} = 0.9537$. The inset illustrates in detail the distribution of spin vectors and skyrmionic numbers corresponding to different order modes, where the blue dashed circles represent the boundary of spin skyrmions.

In summary, we theoretically propose and experimentally observe that the Néel-type spin skyrmions can be realized on the surface of 3D concentric cylindrical structures. By setting up four loudspeakers with different phases to form a spin source for excitation, we analyze the relationship between the time-averaged energy flux $\mathcal{J}$ and the reactive power vector $\mathcal{R}$, and then obtain the vector distribution of the corresponding acoustic spin density $\boldsymbol{s}$. With opposite evanescent directions at the top and bottom surfaces, the spin distributions showcase dispersive and convergent configurations with the same skyrmionic number, accordingly. Finally, we propose a scheme to improve the configuration of the spin skyrmionic mode by setting the hard boundary at the structure edge. In this work, the experimentally observed spin skyrmion not only expands the family of acoustic topological textures but also holds great potential applications for manipulating small particles in the structural acoustic fields.

See the supplementary material for more information, including the mapping relationship of the spin skyrmion mode, the simulation results of the third-order Néel-type spin skyrmion mode, the simulation results with the clockwise acoustic spin source as the excitation source, and the quantitative analysis of specific Q factor variation results.

This work was supported by the Scientific research projects of colleges and universities in Anhui Province (Grant Nos. 2022AH040114) and the University Synergy Innovation Program of Anhui Province (Grant No. GXXT-2022-015).

AUTHOR DECLARATIONS

Conflict of Interest

The authors have no conflicts to disclose.

Author Contributions

Jia-Yu Zheng: Investigation (equal); Validation (equal); Visualization (equal); Writing – original draft (equal). **Wan-Na Chen:** Investigation (equal); Validation (equal); Writing – review & editing (equal). **Jing-Yi Lv:** Visualization (equal); Writing – review & editing (equal). **Lei Wang:** Formal analysis (equal); Visualization (equal). **Hua-Feng Xu:** Validation (equal); Visualization (equal); Writing – review & editing (equal). **Hong-Wei Wu:** Conceptualization (equal); Formal analysis (equal); Funding acquisition (equal); Investigation (equal); Supervision (equal); Validation (equal); Visualization (equal); Writing – original draft (equal); Writing – review & editing (equal).

DATA AVAILABILITY

The data that support the findings of this study are available from the corresponding author upon reasonable request.

REFERENCES

[1] T. H. R. Skyrme, Nucl. Phys. **31**, 556 (1962).
[2] I. Kézsmárki, S. Bordács, P. Milde, E. Neuber, L. M. Eng, J. S. White, H. M. Rønnow, C. D. Dewhurst, M. Mochizuki, K. Yanai, H. Nakamura, D. Ehlers, V. Tsurkan, and A. Loidl, Nat. Mater. **14**, 1116 (2015).
[3] J. Jena, B. Göbel, T. P. Ma, V. Kumar, R. Saha, I. Mertig, C. Felser, and S. S. P. Parkin, Nat. Commun. **11**, 1115 (2020).
[4] A. K. Nayak, V. Kumar, T. P. Ma, P. Werner, E. Pippel, R. Sahoo, F. Damay, U. K. Rößler, C. Felser, and S. S. P. Parkin, Nature **548**, 561 (2017).
[5] A. Ghosh, S. Yang, Y. Dai, Z. K. Zhou, T. Y. Wang, C. B. Huang, and H. Petek, Appl. Phys. Rev. **8**, 041413 (2021).
[6] C. F. Lu, B. Wang, X. Fang, D. P. Tsai, W. M. Zhu, Q. H. Song, X. Deng, T. He, X. Y. Gong, H. Luo, Z. S. Wang, X. H. Dai, Y. Z. Shi, and X. B. Cheng, Nano Lett. **24**, 104 (2024).
[7] M. Król, H. Sigurdsson, K. Rechcińska, P. Oliwa, K. Tyszka, W. Bardyszewski, A. Opala, M. Matuszewski, P. Morawiak, R. Mazur, W. Piecek, P. Kula, P. G. Lagoudakis, B. Pietka, and J. Szczytko, Optica **8**, 255 (2021).
[8] L. Desplat, J.-V. Kim, and R. Stamps, Phys. Rev. B **99**, 174409 (2019).
[9] S. Bera and S. S. Mandal, Phys. Rev. Res. **1**, 033109 (2019).
[10] H. W. Wang and S. H. Fan, Phys. Rev. Lett. **131**, 263801 (2023).
[11] X. S. Wang, A. Qaiumzadeh, and A. Brataas, Phys. Rev. Lett. **123**, 147203 (2019).
[12] S. Tsesses, E. Ostrovsky, K. Cohen, B. Gjonaj, N. H. Lindner, and G. Bartal, Science **361**, 993 (2018).
[13] Y. J. Shen, Q. Zhang, P. Shi, L. P. Du, X. C. Yuan, and A. V. Zayats, Nat. Photonics **18**, 15 (2024).
[14] Q. Zhang, Z. W. Xie, L. P. Du, P. Shi, and X. C. Yuan, Phys. Rev. Res. **3**, 023109 (2021).
[15] Q. Zhang, Z. W. Xie, P. Shi, H. Yang, H. R. He, L. P. Du, and X. C. Yuan, Photonics Res. **10**, 947 (2022).
[16] R. Tamura, P. Kumar, A. S. Rao, K. Tsuda, F. Getzlaff, K. Miyamoto, N. M. Litchinitser, and T. Omatsu, APL Photonics **9**, 046104 (2024).
[17] S. Cao, L. P. Du, P. Shi, and X. C. Yuan, Opt. Express **32**, 4167 (2024).
[18] S. Wang, Z. Zhou, Z. Zheng, J. Sun, H. Cao, S. Song, Z. L. Deng, F. Qin, Y. Cao, and X. Li, Phys. Rev. Lett. **133**, 073802 (2024).
[19] J. Ma, J. Yang, S. Liu, B. Chen, X. Li, C. Song, G. Qiu, K. Zou, X. Hu, F. Li, Y. Yu, and J. Liu, Nat. Phys. **21**, 1462 (2025).
[20] P. Ornelas, I. Nape, R. de Mello Koch, and A. Forbes, Nat. Photonics **18**, 258 (2024).
[21] H. Ge, X. Y. Xu, L. Liu, R. Xu, Z. K. Lin, S. Y. Yu, M. Bao, J. H. Jiang, M. H. Lu, and Y. F. Chen, Phys. Rev. Lett. **127**, 144502 (2021).
[22] R. D. Muelas-Hurtado, K. Volke-Sepúlveda, J. L. Ealo, F. Nori, M. A. Alonso, K. Y. Bliokh, and E. Brasselet, Phys. Rev. Lett. **129**, 204301 (2022).
[23] L. Y. Cao, S. Wan, Y. Zeng, Y. F. Zhu, and B. Assouar, Sci. Adv. **9**, eadf3652 (2023).
[24] D. A. Smirnova, F. Nori, and K. Y. Bliokh, Phys. Rev. Lett. **132**, 054003 (2024).
[25] B. Wang, Z. Che, C. Cheng, C. Tong, L. Shi, Y. Shen, K. Y. Bliokh, and J. Zi, Nature **638**, 394 (2025).
[26] N. Zhou, W. N. Chen, W. J. Sun, Z. Q. Sheng, and H. W. Wu, Appl. Phys. Lett. **125**, 042204 (2024).
[27] P. Hu, H. W. Wu, W. J. Sun, N. Zhou, X. Chen, Y. Q. Yang, and Z. Q. Sheng, Appl. Phys. Lett. **122**, 022201 (2023).

[28] W. J. Sun, H. W. Wu, P. Hu, N. Zhou, X. Chen, Y. Q. Yang, and Z. Q. Sheng, Appl. Phys. Lett. **122**, 202201 (2023).
[29] W. N. Chen, H. W. Wu, J. Y. Lv, J. Y. Zheng, W. B. Zhang, N. Zhou, and Z. Q. Sheng, Phys. Rev. B **111**, 174302 (2025).
[30] W. J. Sun, N. Zhou, W. N. Chen, Z. Q. Sheng, and H. W. Wu, Adv. Sci. **11**, 2401370 (2024).
[31] Y. Long, H. Ge, D. Zhang, X. Xu, J. Ren, M. H. Lu, M. Bao, H. Chen, and Y. F. Chen, Natl. Sci. Rev. **7**, 1024 (2020).
[32] K. Y. Bliokh and F. Nori, Phys. Rev. B **99**, 020301 (2019).
[33] Y. Long, C. Yang, H. Chen, and J. Ren, Phys. Rev. Appl. **19**, 064053 (2023).
[34] P. X. Xie, Z. Q. Sheng, Z. X. Huang, P. Hu, and H. W. Wu, Appl. Phys. Lett. **122**, 222202 (2023).